

Bulk spin-orbit torque-driven spin Hall nano-oscillators using PtBi alloys

Utkarsh Shashank¹, Akash Kumar^{1,2,3}, Tahereh Sadat Parvini^{4,5,6}, Hauke Heyen⁴, Lunjie Zeng⁷, Andrew B. Yankovich⁷, Mona Rajabali⁸, Eva Olsson⁷, Markus Münzenberg^{*4}, and Johan Åkerman^{†1,2,3}

¹Applied Spintronics Group, Department of Physics, University of Gothenburg, 412 96 Gothenburg, Sweden

²Research Institute of Electrical Communication, Tohoku University, Sendai, Japan

³Center for Science and Innovation in Spintronics, Tohoku University, Sendai, Japan

⁴Institut für Physik, Universität Greifswald, 17489 Greifswald, Germany

⁵Walther-Meißner-Institut, Bayerische Akademie der Wissenschaften, 85748 Garching, Germany

⁶Munich Center for Quantum Science and Technology (MCQST), Munich, Germany

⁷Department of Physics, Chalmers University of Technology, 412 96 Gothenburg, Sweden

⁸NanOsc AB, Kista, Sweden

Keywords: spin-orbit torque, spin Hall effect, spin Hall nano-oscillator, auto-oscillation, extrinsic side-jump scattering

Abstract

Spin-orbit-torque-driven auto-oscillations in spin Hall nano-oscillators (SHNOs) offer a transformative pathway toward energy-efficient, nanoscale microwave devices for next-generation neuromorphic computing and high-frequency technologies. A key requirement for achieving robust, sustained oscillations is reducing the threshold current (I_{th}), strongly governed by spin Hall efficiency (θ_{SH}). However, conventional strategies to enhance θ_{SH} face trade-offs, including high longitudinal resistivity, interfacial effects,

^{*}markus.muenzenberg@uni-greifswald.de

[†]johan.akerman@physics.gu.se

and symmetry-breaking torques that limit performance. Here, we demonstrate a substantial enhancement of the bulk spin Hall effect in PtBi alloys, achieving over a three-fold increase in θ_{SH} , from 0.07 in pure Pt to 0.24 in Pt_{94.0}Bi_{6.0} and 0.19 in Pt_{91.3}Bi_{8.7}, as extracted from DC-bias spin-torque ferromagnetic resonance. The enhanced θ_{SH} originates from bulk-dominated, extrinsic side-jump scattering across all PtBi compositions. Correspondingly, we observe a 42% and 32% reduction in I_{th} in 100 nm SHNOs based on Co₄₀Fe₄₀B₂₀(3 nm)/Pt_{94.0}Bi_{6.0}(4 nm) and Co₄₀Fe₄₀B₂₀(3 nm)/Pt_{91.3}Bi_{8.7}(4 nm), respectively. Structural characterization reveals reduced Pt crystallinity, along with emergence of preferred crystallographic orientations upon introducing higher Bi concentrations. Together, these results position PtBi alloys as a compelling alternative to conventional 5d transition metals, enabling enhanced θ_{SH} and significantly lower I_{th} , thus opening new avenues for energy-efficient neuromorphic computing and magnetic random access memory.

1 Introduction

The efficient control of magnetization via spin-orbit torque (SOT) [1], primarily generated by the Spin Hall effect (SHE) [2, 3], lies at the core of modern spintronics [4]. It plays a key role in magnetization switching [5, 6, 7, 8], in the generation and control of propagating spin waves [9, 10], in spin Hall nano-oscillators (SHNOs) [11, 12], and in the movement of domain walls and skyrmions [13, 14, 15]. In a heavy metal (HM) with large spin-orbit coupling, the SHE generates a sizeable transverse spin current density, \mathbf{j}_s , from a longitudinal charge current density, \mathbf{j}_c . The generated \mathbf{j}_s can exert different torques on the magnetization of an adjacent ferromagnet (FM) layer, where the damping-like torque, $\boldsymbol{\tau}_{\text{DL}}$, is the component collinear with the usual damping, $\boldsymbol{\tau}_\alpha$, of the FM layer [16]. If $\boldsymbol{\tau}_{\text{DL}}$ balances $\boldsymbol{\tau}_\alpha$, the threshold condition for FM auto-oscillations (AO), with a corresponding threshold current (I_{th}), is reached in the SHNO [17, 18].

Over the past decade, SOT-driven nanoconstriction-based SHNOs have garnered significant attention thanks to their straightforward nano-fabrication, direct optical and gate access to the auto-oscillating FM region, and a rich magneto-dynamical behavior [19]. SHNOs have shown tremendous promise for mutual synchronization in chains [20, 21] and arrays [22, 23, 24], paving the way for applications in neuromorphic computing [25, 26, 27], Ising machines [28], magnonic conduits [10] and high frequency GHz technologies [29].

To reduce I_{th} , a higher conversion of \mathbf{j}_c to \mathbf{j}_s , defined as the spin Hall efficiency, θ_{SH} , is required. θ_{SH} can be expressed as $\mathbf{j}_s = \frac{\hbar}{2e} \theta_{\text{SH}} (\mathbf{j}_c \times \hat{\boldsymbol{\sigma}})$, where $\hat{\boldsymbol{\sigma}}$ is the polarization of the spin current, e is the elementary charge, and \hbar is the reduced Planck constant, and the most commonly used HM Pt has a moderate $\theta_{\text{SH}} \approx 0.05$ -0.09, from its intrinsic SHE [30]. Ion-implantation [31, 32, 33, 34] or sputtering [35, 36, 37] of non-metallic lighter impurities, such as S, O, N, P can also be used to tune the θ_{SH} of Pt, Ta, W. However, such tuning requires careful materials engineering and often comes with a trade-off in the form of increased longitudinal resistivity (ρ_{xx}), as observed in TaN, which can exhibit values as high as 3000 $\mu\Omega\cdot\text{cm}$ [37]. In contrast, metallic impurities introduced by co-sputtering with the HM, neither require complex engineering nor introduce drastic changes in ρ_{xx} . A better trade-off between θ_{SH} and ρ_{xx} , is crucial for low-power consumption in SOT magnetic random access memory (SOT-MRAM) [34, 38]. In this context, Pt, Ta, and W based alloys have been explored (θ_{SH}

values in parentheses), such as $\text{Pt}_{28}\text{Cu}_{72}$ (0.07) [39], $\text{Pt}_{45}\text{Pd}_{55}$ (0.06) [40], $\text{Pt}_{92}\text{Bi}_8$ (0.10) [41]; $\text{W}_{100-x}\text{Ta}_x$ (-0.35 to -0.62) [42], and $\text{Cu}_{100-x}\text{Ta}_x$ (-0.04 to -0.09) [37]. Within this framework, Hayashi *et al.* showed that $\text{Pt}_{100-x}\text{Bi}_x/\text{Co}$ bilayers with substantial Bi concentrations ($x = 25\text{--}50$) exhibit markedly improved θ_{SH} and reduced switching current densities relative to pure Pt, identifying PtBi as a strong candidate for energy-efficient magnetization switching [43]. Complementing this, Münzenberg *et al.* demonstrated that $\text{Pt}_{92}\text{Bi}_8$ -based hetero-structures can act as high-performance THz spintronic emitters, delivering broader bandwidths and higher central frequencies than conventional bilayer systems [44]. In addition, at higher Bi concentrations—such as in stoichiometric PtBi₂—this material has attracted attention as a topological system, exhibiting giant three-dimensional Rashba-like spin splitting ($\alpha_{\text{R}} \approx 4.36 \text{ eV} \cdot \text{\AA}$) [45] and surface-bound superconducting gaps reaching up to 20 meV [46]. Despite these advances, a unified understanding of the reciprocal connection between θ_{SH} and I_{th} in $\text{Pt}_{100-x}\text{Bi}_x$ alloys—via both ST-FMR and direct AO measurements—remains unexplored.

Here, we report on a dramatic increase in θ_{SH} by more than three times when alloying Pt with Bi, and a corresponding decrease of I_{th} by 42% in SHNOs based on $\text{Pt}_{94.0}\text{Bi}_{6.0}$ and $\text{Co}_{40}\text{Fe}_{40}\text{B}_{20}$. We deposited $\text{Pt}_{100-x}\text{Bi}_x$ alloy thin films using electron-beam co-evaporation and systematically varied the Bi concentrations across $x = 0.0, 3.9, 6.0$, and 8.7 (hereafter denoted as Pure Pt, $\text{Pt}_{96.1}\text{Bi}_{3.9}$, $\text{Pt}_{94.0}\text{Bi}_{6.0}$, and $\text{Pt}_{91.3}\text{Bi}_{8.7}$, respectively). Structural characterization by grazing-incidence X-ray diffraction (GIXRD) reveals a progressive loss of crystallinity with increasing Bi content, suggesting enhanced scattering contributions. Cross-sectional transmission electron microscopy (TEM) indicates a reduction in crystallinity of Pt, and a uniform distribution of Bi in Pt. Linewidth analysis of DC-biased spin-torque ferromagnetic resonance (ST-FMR) measurements *vs.* current yields a sharp increase in θ_{SH} from 0.07 ± 0.01 in pure Pt to 0.24 ± 0.02 and 0.19 ± 0.01 in the $\text{Pt}_{94.0}\text{Bi}_{6.0}$ and $\text{Pt}_{91.3}\text{Bi}_{8.7}$ alloys, respectively. To rule out artifacts and confirm the bulk origin of SOT, we demonstrate a clear $\sin 2\phi \cos \phi$ in-plane angular dependence of the SOT for all PtBi alloys. Thanks to the increase in θ_{SH} , we observe a 42% and 32% reduction in I_{th} for $\text{Pt}_{94.0}\text{Bi}_{6.0}$ and $\text{Pt}_{91.3}\text{Bi}_{8.7}$ based 100 nm SHNOs. Our findings of a higher θ_{SH} driven by bulk-extrinsic SHE, accompanied by a reduced I_{th} , establish Bi alloying in Pt as a robust strategy for engineering energy-efficient SHNOs, opening new avenues beyond conventional 5d transition metals.

2 Results and Discussion

2.1 Structural Characterization via GIXRD and TEM

Figure 1a shows Grazing incidence X-ray Diffraction (GIXRD) patterns of $\text{Pt}_{100-x}\text{Bi}_x$ thin films (see Experimental Section). Reflections from the (111), (200), (220), and (311) planes confirm a polycrystalline face-centered cubic (*fcc*) phase in pure Pt and $\text{Pt}_{96.1}\text{Bi}_{3.9}$ [34, 47]. Increasing the Bi content reduces the overall reflection intensities, particularly that of the (220) peak, indicating a reduction in crystallinity [34, 48, 49]. Peak broadening becomes more pronounced in $\text{Pt}_{94.0}\text{Bi}_{6.0}$ and $\text{Pt}_{91.3}\text{Bi}_{8.7}$. The intensity ratio $I_{(111)}/I_{(220)}$ rises from 0.39 (Pure Pt) to 1.65 (6% Bi), then falls to 1.07 at 8.7% Bi. Similarly, the lattice parameter increases from 3.953 to 3.966 Å (0–6% Bi), followed by a slight decrease to 3.959 Å at 8.7% Bi. This non-monotonic trend suggests a shift in preferred crystallographic orientation, likely due to

strain-induced texturing at higher Bi concentrations, consistent with previous report [43].

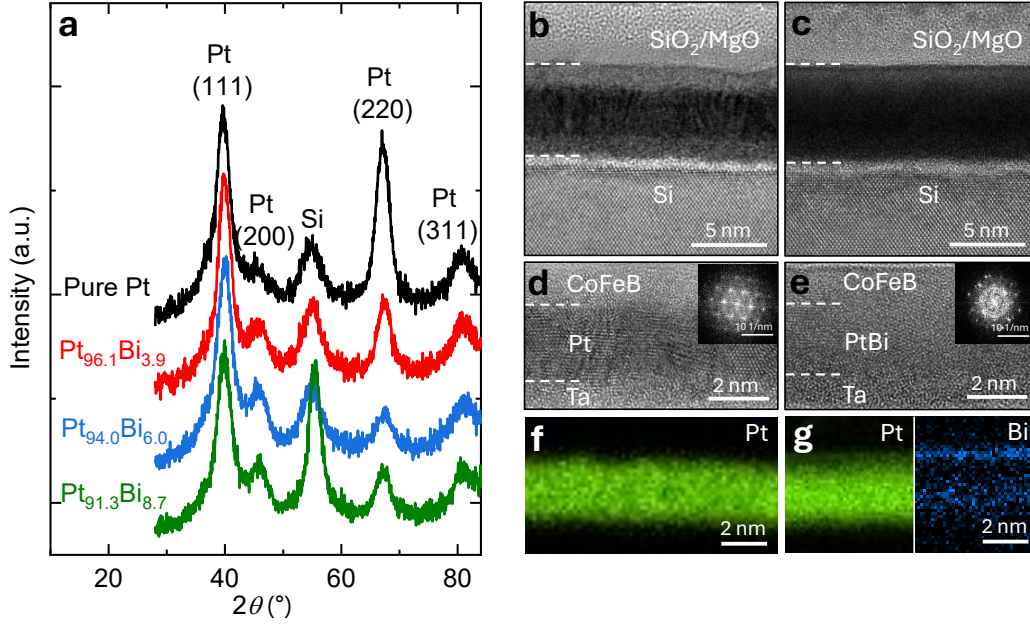


Figure 1: (a) GIXRD patterns of the pure Pt stack (black) and PtBi alloy stacks with compositions $\text{Pt}_{96.1}\text{Bi}_{3.9}$ (red), $\text{Pt}_{94.0}\text{Bi}_{6.0}$ (blue), and $\text{Pt}_{91.3}\text{Bi}_{8.7}$ (green). (b,c) Low-resolution cross-sectional bright-field TEM images of (b) the pure Pt stack (HR-Si/Ta(2.4 nm)/Pt(4.0 nm)/ $\text{Co}_{40}\text{Fe}_{40}\text{B}_{20}$ (3.0 nm) and (c) the $\text{Pt}_{94.0}\text{Bi}_{6.0}$ stack (HR-Si/Ta(2.4 nm)/ $\text{Pt}_{94.0}\text{Bi}_{6.0}$ (4.0 nm)/ $\text{Co}_{40}\text{Fe}_{40}\text{B}_{20}$ (3.0 nm)) both showing uniform, well-defined layers with comparable total thicknesses. Both layers are capped with MgO (2.0 nm)/ SiO_2 (3.0 nm). (d,e) High-resolution TEM images of the same stacks. (d) The pure Pt stack shows clear lattice fringes and sharp Bragg spots (inset FFT), indicative of a polycrystalline Pt structure. (e) The $\text{Pt}_{94.0}\text{Bi}_{6.0}$ stack displays reduced fringe contrast and weaker Bragg spots (inset), suggesting lower crystallinity or a change in preferred orientation. (f,g) EDS elemental maps of Pt and Bi from HAADF-STEM for the pure Pt and $\text{Pt}_{94.0}\text{Bi}_{6.0}$ stacks, respectively. Bi is uniformly distributed within the $\text{Pt}_{94.0}\text{Bi}_{6.0}$ layer, with slight enrichment at the PtBi/ $\text{Co}_{40}\text{Fe}_{40}\text{B}_{20}$ interface. Additional HAADF-STEM images and full elemental maps are provided in Supporting Information S1 and S2.

Figure 1b,c display low-resolution cross-sectional bright-field TEM images of the pure Pt stack and the $\text{Pt}_{94.0}\text{Bi}_{6.0}$ stack, respectively. Both stacks exhibit well-defined, uniform layer structures with comparable total thicknesses. Figures 1d,e present high-resolution bright-field TEM images of the same samples. In the pure Pt sample (Figure 1d), clear lattice fringes are visible, and the fast Fourier transform (FFT) analysis (inset) shows distinct Bragg spots and a clear ring, indicating a polycrystalline structure of the Pt layer [31, 34, 50]. In contrast, the $\text{Pt}_{94.0}\text{Bi}_{6.0}$ sample (Figure 1e) exhibits weaker lattice fringes and diminished Bragg spots (inset), suggesting reduced crystallinity or a shift in preferred crystallographic orientation, consistent with the GIXRD results. Figure 1f,g provide Energy-dispersive X-ray spectroscopy (EDS) elemental maps from High-angle annular dark field scanning transmission electron

microscopy (HAADF-STEM) for the same samples. In the $\text{Pt}_{94.0}\text{Bi}_{6.0}$ stack (Figure 1g, right panel), Bi is uniformly distributed throughout the target Pt layer, with no sign of clustering. A modest enrichment of Bi is also observed at the $\text{Pt}_{94.0}\text{Bi}_{6.0}/\text{Co}_{40}\text{Fe}_{40}\text{B}_{20}$ interface. The impact of both bulk and interfacial Bi distributions on the SHE in Pt will be addressed in subsequent sections.

2.2 Spin-torque ferromagnetic resonance measurements

To evaluate how Bi doping modulates the SHE in Pt, we performed spin-torque ferromagnetic resonance (ST-FMR) measurements [16] (see Experimental section for details). **Figure 2a** illustrates the schematic of the ST-FMR measurement and Figure 2b shows the experimental setup. An in-plane microwave current I_{rf} with a power of 4 dBm was applied along the x-axis of the HM/FM bilayer via a ground-source-ground (GSG) coplanar waveguide (CPW). The external magnetic field H_{ext} was swept ± 500 mT at an angle $\phi = 70^\circ$ between I_{rf} and H_{ext} . The charge current density \mathbf{j}_c (x-axis) driven by I_{rf} generates a spin current density \mathbf{j}_s along the z-axis with spin polarization $\hat{\sigma}$ along the y-axis. This \mathbf{j}_s exerts an in-plane $\boldsymbol{\tau}_{\text{DL}}$ on the magnetization \mathbf{m} of the FM layer. Simultaneously, the Oersted field, h_{rf} , generated by I_{rf} acts as an out-of-plane Oersted field torque, $\boldsymbol{\tau}_{\text{OF}}$. Interfacial effects, rather than bulk mechanisms, can also induce out-of-plane field-like torques ($\boldsymbol{\tau}_{\text{FL}}$) arising from the Rashba effect, particularly in thinner FM layers ($\lesssim 1$ nm) interfaced with HM [51, 52], which may overlap with $\boldsymbol{\tau}_{\text{OF}}$. When $\boldsymbol{\tau}_{\text{FL}}$ is small, as in bulk SHE heterostructures, the combined torques ($\boldsymbol{\tau}_{\text{DL}}$ and $\boldsymbol{\tau}_{\text{OF}}$) govern the magnetization precession. The precession of \mathbf{m} around the effective field H_{eff} induces a time-dependent resistance variation via the anisotropic magnetoresistance (AMR), $\Delta R \propto \cos^2 \phi$ (see Supporting Information S3). Mixing with I_{rf} , the varying ΔR generates a rectified ST-FMR voltage, V_{dc} . The I_{rf} was amplitude modulated at 98.76 Hz, serving as a reference signal for lock-in detection (see Figure 2b).

Figure 2c shows the ST-FMR voltage spectrum measured at $f = 8$ GHz and $I_{\text{dc}} = 0$ mA for $\text{Pt}_{94.0}\text{Bi}_{6.0}$. The measured V_{dc} is defined as [16]:

$$V_{\text{dc}} = SF_{\text{sym}}(H_{\text{ext}}) + AF_{\text{asym}}(H_{\text{ext}}), \quad (1)$$

where, $F_{\text{sym}}(H_{\text{ext}}) = \frac{(\Delta H)^2}{(\mu_0 H_{\text{ext}} - \mu_0 H_{\text{R}})^2 + (\Delta H)^2}$ is the symmetric (Lorentzian) component, and $F_{\text{asym}}(H_{\text{ext}}) = \frac{\Delta H(\mu_0 H_{\text{ext}} - \mu_0 H_{\text{R}})}{(\mu_0 H_{\text{ext}} - \mu_0 H_{\text{R}})^2 + (\Delta H)^2}$ is the antisymmetric (dispersive) component. The parameters S and A are the weight factors corresponding to the symmetric and antisymmetric components, respectively. ΔH and H_{R} are the linewidth (half-width-at-half-maximum) and resonance field of the ST-FMR spectra, respectively. Strikingly, a very high symmetric component $SF_{\text{sym}}(H_{\text{ext}})$ confirming the high $\boldsymbol{\tau}_{\text{DL}}$ is observed for $\text{Pt}_{94.0}\text{Bi}_{6.0}$. Furthermore, in-plane angular ST-FMR measurements reveal that both the S and A weight factors exhibit a clear $\sin 2\phi \cos \phi$ dependence across all $\text{Pt}_{100-x}\text{Bi}_x$ compositions (see Supporting Information S4 for details). This angular dependence is a characteristic of a conventional bulk-SOT origin, free from torque symmetry-breaking, and rules out significant contributions from experimental artifacts [34, 53, 54].

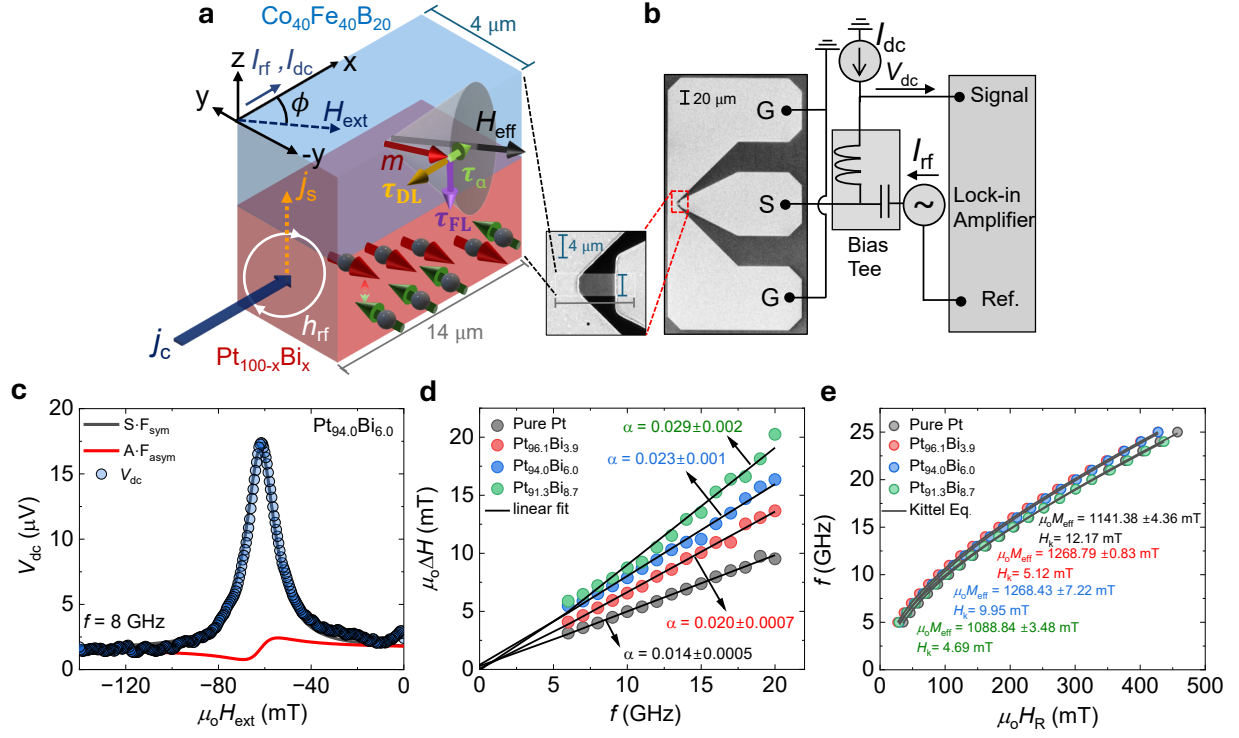


Figure 2: a) Schematic of the SHE and the microscopic mechanism of the ST-FMR excitation, depicting the torques acting on the FM magnetization. b) The ST-FMR measurement technique and detection principle along with the micro-bar device connected to a GSG-CPW. A zoom-in SEM image of the red square shows the micro-bar. c) ST-FMR voltage (V_{dc}) at $f = 8$ GHz of Pt_{94.0}Bi_{6.0}, with separate symmetric and antisymmetric components fit to Eq. (1). d) ΔH vs f for $f = 6$ –20 GHz, with solid black lines being linear fits to Equation (2). e) f vs. H_{R} for all samples evaluated in this study. Solid lines in (e) represent fits to the Kittel Equation (3).

Next, we extract the Gilbert damping parameter α by plotting ΔH as a function of f (see Figure 2d), using the relation

$$\Delta H = \Delta H_0 + \frac{2\pi\alpha}{\gamma\mu_0}f, \quad (2)$$

where ΔH_0 denotes the f -independent inhomogeneous linewidth broadening [55], and γ is the gyromagnetic ratio. A systematic increase in α is observed from 0.014 ± 0.0005 (pure Pt) to 0.020 ± 0.0007 , 0.023 ± 0.001 and 0.029 ± 0.002 for Pt_{96.1}Bi_{3.9}, Pt_{94.0}Bi_{6.0}, and Pt_{91.3}Bi_{8.7}, respectively. This trend reflects enhanced spin current generation, potentially arising from spin pumping [41] and/or an increase in SHE [32, 33]. The extracted ΔH_0 remains low and positive (0.2–2.1 mT), indicating excellent film quality [31, 32]. Figure 2e depicts the frequency dependence of the resonance field, H_{R} using the Kittel formula:

$$f = \frac{\gamma\mu_0}{2\pi} \sqrt{(H_{\text{R}} + H_{\text{K}})(H_{\text{R}} + H_{\text{K}} + M_{\text{eff}})}, \quad (3)$$

where, H_k is in-plane magnetic anisotropy field and M_{eff} is effective demagnetization [56]. The extracted M_{eff} values—1141.4 mT (pure Pt), 1268.8 mT ($\text{Pt}_{96.1}\text{Bi}_{3.9}$), 1268.4 mT ($\text{Pt}_{94.0}\text{Bi}_{6.0}$), and 1088.8 mT ($\text{Pt}_{91.3}\text{Bi}_{8.7}$)—along with H_K values of 4–12 mT, confirm no significant variation in magnetic properties upon Bi incorporation.

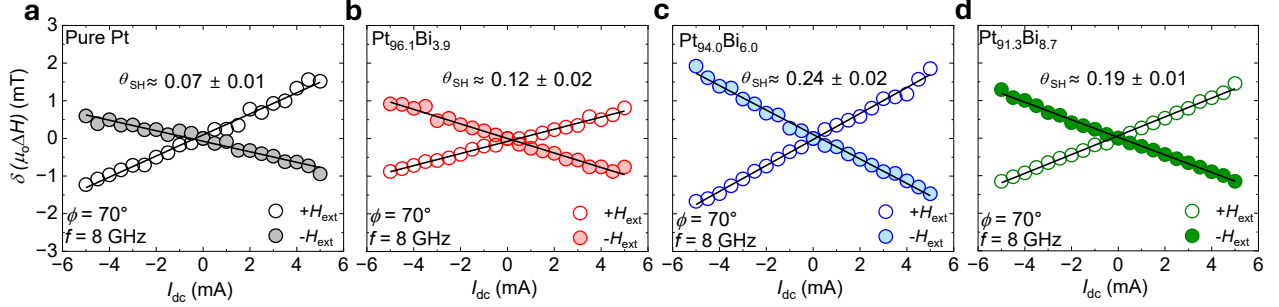


Figure 3: Current-induced modulation of linewidth, $\delta(\mu_0\Delta H)$ as a function of I_{dc} at $f = 8$ GHz for a) Pure Pt, b) $\text{Pt}_{96.1}\text{Bi}_{3.9}$, c) $\text{Pt}_{94.0}\text{Bi}_{6.0}$, and d) $\text{Pt}_{91.3}\text{Bi}_{8.7}$. Open circles correspond to positive magnetic field sweep ($+H_{\text{ext}}$), while filled circles correspond to negative sweep ($-H_{\text{ext}}$). The solid black lines are linear fits. The increasing slope of $\delta(\mu_0\Delta H)/I_{\text{dc}}$ with Bi impurity in Pt, indicates enhanced θ_{SH} .

To quantify θ_{SH} , we use DC-bias ST-FMR [16], where a direct current I_{dc} is applied simultaneously with I_{rf} (see Figure 2b) under an external magnetic field H_{ext} , to modulate the linewidth ΔH . **Figure 3a–d** show the change in linewidth, $\delta(\mu_0\Delta H)$, as a function of I_{dc} at $f = 8$ GHz, measured at an angle $\phi = 70^\circ$ with an input power of 4 dBm. Here, ϕ is the angle between the combined current direction ($I_{\text{rf}} + I_{\text{dc}}$) and the external field H_{ext} . The angle $\phi = 70^\circ$ was chosen to maximize the linewidth modulation since $\sin \phi$ reaches near its peak between $70 - 75^\circ$, and the AMR also exhibits significant variation within the $45^\circ - 75^\circ$ range [18, 57] fruitful for a clean ST-FMR spectrum (see Equation 4). The change in linewidth is defined as $\delta(\mu_0\Delta H) = \mu_0\Delta H|_{I_{\text{dc}}} - \mu_0\Delta H|_{I_{\text{dc}}=0}$, which varies linearly with I_{dc} . We then define the effective current-dependent damping parameter, α_{eff} given as $\alpha_{\text{eff}} = \frac{\gamma}{2\pi f} \delta(\mu_0\Delta H)$. Reversing the polarity of H_{ext} from ($+H_{\text{ext}}$) $\phi=70^\circ$ to ($-H_{\text{ext}}$) at $\phi=250^\circ$ reverses the magnetization direction of $\text{Co}_{40}\text{Fe}_{40}\text{B}_{20}$, which correspondingly reverses the slope of $\delta(\mu_0\Delta H)/I_{\text{dc}}$, confirming the conventional SHE induced SOT [58]. Using a parallel resistor model (see Supporting Information S5 for details on calculating ρ_{xx}), we estimate the current density in the HM layer, $j_{\text{dc,HM}}$, and extract θ_{SH} from the slope $\frac{\Delta\alpha_{\text{eff}}}{\Delta j_{\text{dc,HM}}}$ according to [16]:

$$\theta_{\text{SH}} = \left[\frac{2e}{\hbar} \left(H_0 + \frac{M_{\text{eff}}}{2} \right) \mu_0 M_s t \left| \frac{\Delta\alpha_{\text{eff}}}{\Delta j_{\text{dc,HM}}} \right| \right] / \sin \phi, \quad (4)$$

where M_s and t are the saturation magnetization and thickness of $\text{Co}_{40}\text{Fe}_{40}\text{B}_{20}$, respectively, and M_{eff} is the effective demagnetization obtained from Kittel fitting [55, 59] (see Figure 2e). We observe a slight increase in θ_{SH} from 0.07 ± 0.01 (Pure Pt) to 0.12 ± 0.02 ($\text{Pt}_{96.1}\text{Bi}_{3.9}$), with a small doping of 3.9%. However, increasing the Bi concentration to 6.0 % and 8.7 % yields a remarkable enhancement in θ_{SH} to 0.24 ± 0.02 ($\text{Pt}_{94.0}\text{Bi}_{6.0}$) and 0.19 ± 0.01 ($\text{Pt}_{91.3}\text{Bi}_{8.7}$). In particular, the highest θ_{SH} occurs at higher Bi concentrations where Pt loses its crystalline

texture, as seen in Figure 1. This supports the correlation between reduced crystallinity and enhanced θ_{SH} in $5d$ transition metals. Recent experimental studies by Parkin *et al.* [38] and Fukuma *et al.* [34] have similarly demonstrated that θ_{SH} peaks near the crystalline-amorphous boundary, where extrinsic scattering from impurities is maximized, which we will explore in later sections.

2.3 Spin Hall nano-oscillators

We fabricated 100 nm wide SHNOs (see Experimental Section for details) and measured AO on all $\text{Pt}_{100-x}\text{Bi}_x/\text{Co}_{40}\text{Fe}_{40}\text{B}_{20}$ hetero-structures to observe the effect of a higher θ_{SH} on I_{th} . A schematic of the setup is shown in **Figure 4a**. A direct current, I_{dc} (along the x-axis) was applied through a Bias Tee, while the resulting microwave signals were extracted through the high-frequency port, amplified using a low-noise amplifier (LNA), and analyzed with a spectrum analyzer (SA). A moderate out-of-plane field ($\theta=84^\circ$) was selected to achieve a weak negative nonlinearity [60]. The in-plane angle, $\phi=20^\circ$, was chosen to ensure adequate electrical sensitivity of the signal (ϕ is the angle between the y-axis and H_{ext}).

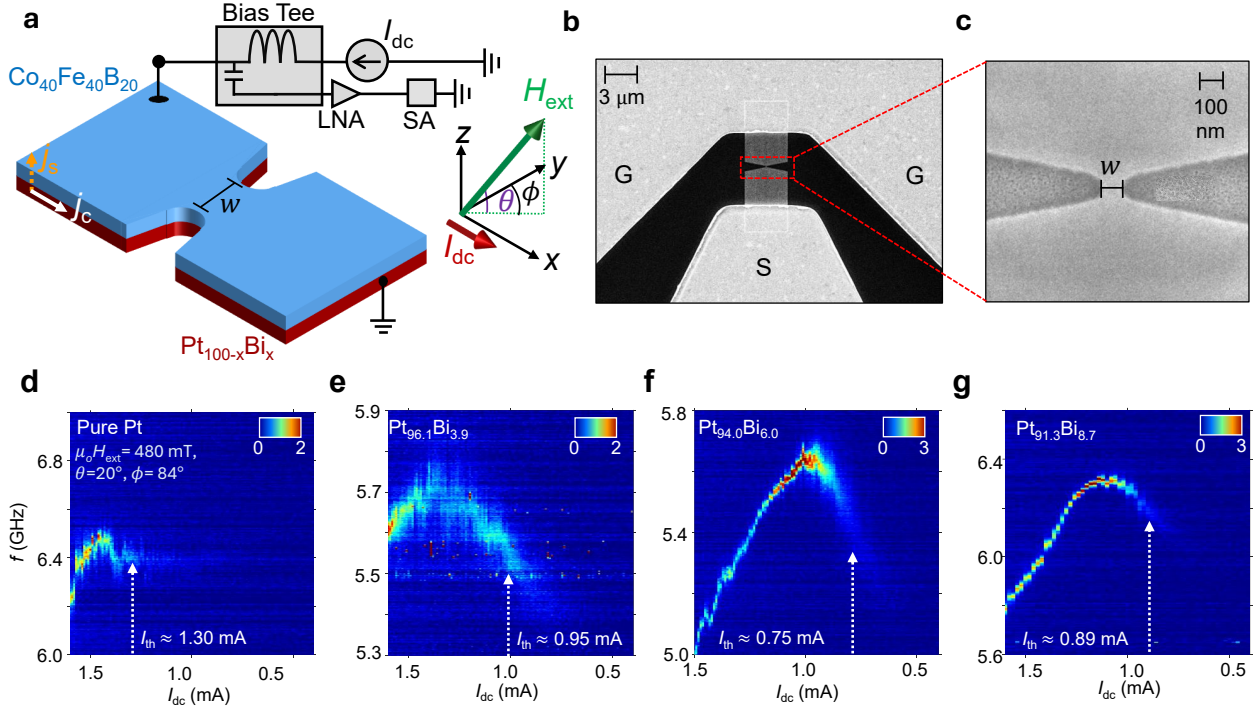


Figure 4: a) Schematic of the SHNO and measurement setup. b) SEM image of the GSG-based CPW with SHNO. c) Enlarged SEM of the 100 nm wide SHNO (black scale bars in b,c). PSD from the 100 nm SHNO as a function of I_{dc} at $\mu_0 H_{\text{ext}} = 480$ mT, $\phi = 20^\circ$, $\theta = 84^\circ$ for d) Pure Pt, e) $\text{Pt}_{96.1}\text{Bi}_{3.9}$, f) $\text{Pt}_{94.0}\text{Bi}_{6.0}$, and g) $\text{Pt}_{91.3}\text{Bi}_{8.7}$. Color bars indicate peak power (dB above noise floor). The white arrows mark respective I_{th} .

Figure 4b shows the scanning electron microscope (SEM) image of the device under test,

and Figure 4c presents the enlarged SEM image of the 100 nm wide SHNO. The actual measured width w is in good agreement with the nominal design value. To understand the reciprocal relationship between the enhancement in θ_{SH} and the reduction in I_{th} , we performed current-dependent AO and extracted the Power Spectral Density (PSD) generated by the 100 nm wide SHNO under $\mu_o H_{\text{ext}} = 480$ mT ($\phi=20^\circ$ and $\theta=84^\circ$) for all samples, as shown in Figure 4d-g. A non-monotonic current dependence of the AO frequency is observed, attributed to a localized AO “bullet” mode promoted by negative nonlinearity, \mathcal{N} , typical for a FM layer with its magnetization far from the film normal [60]. The I_{th} is 1.30 mA for pure Pt, decreasing to 0.95 mA for Pt_{96.1}Bi_{3.9}. At higher Bi concentrations, I_{th} drops significantly to 0.75 mA (42% reduction) for Pt_{94.0}Bi_{6.0} and 0.89 mA (32% reduction) for Pt_{91.3}Bi_{8.7}. Concurrently, the peak and integrated output power increase while the linewidth decreases at higher Bi concentrations compared to pure Pt. See Supporting Information S6 for AMR, S7 for AO at other fields, S8 for I_{th} extraction, and S9 for peak power, output power, and linewidth.

2.4 Reciprocity and mechanism of spin Hall effect in PtBi alloys

Building on the structural analysis and the observed reciprocity between ST-FMR and AO, several key parameters— ρ_{xx} , θ_{SH} , and I_{th} —are analyzed across all Pt_{100-x}Bi_x alloys (see **Figure 5a-c**). For pure Pt and 3.1% Bi doping, θ_{SH} increases from 0.07 to 0.12, with a corresponding rise in ρ_{xx} from 65 to 270 $\mu\Omega \cdot \text{cm}$, reducing I_{th} from 1.30 mA to 0.97 mA. At 6.0% Bi, ρ_{xx} rises marginally to 288 $\mu\Omega \cdot \text{cm}$, while θ_{SH} significantly rises to 0.24, yielding the lowest I_{th} of 0.75 mA. At 8.7% Bi, ρ_{xx} further increases to 301 $\mu\Omega \cdot \text{cm}$, but θ_{SH} saturates and decreases to 0.19, causing I_{th} to slightly rise to 0.89 mA. This interplay between θ_{SH} and ρ_{xx} is critical for minimizing power consumption, expressed by the factor, $\rho_{\text{xx}}/\theta_{\text{SH}}^2$ relevant for SOT-MRAM applications (Supporting Information S5) [34, 38]. The output power is visibly higher at 6% and 8.7% Bi impurity in Pt compared to pure Pt (Figure 4d-g). Notably, linewidth narrows to ≈ 25 MHz at these higher Bi concentrations, likely due to increased ρ_{xx} redirecting current through Co₄₀Fe₄₀B₂₀ enhancing output power and reducing linewidth (Supporting Information S9). Furthermore, despite the increase in α with Bi doping, the enhanced τ_{DL} from the SHE compensates for τ_{α} , leading to a reduction in I_{th} . This reduction would likely have been more significant if α had remained constant or decreased (see Figure 2d), complicating the direct assessment of SOT effects. The actual effect of torque on the AO is thus likely underestimated, and FM layer with lower α , such as GdFeCo [55] could further enhance the reduction in I_{th} .

To elucidate the mechanism underlying the SHE, we examine the electrical conductivity σ_{xx} . Figure 5d shows θ_{SH} *vs.* σ_{xx} , with values lying in the bad-metal/dirty-metal regime ($\sigma_{\text{xx}} \lesssim 10^4 \Omega^{-1}\text{cm}^{-1}$). In this regime, a linear dependence of θ_{SH} on σ_{xx} indicates a dominant intrinsic SHE contribution in Pt as demonstrated by Casanova *et al.* [61]. However, no clear linear trend is observed, suggesting coexistence of intrinsic and extrinsic side-jump scattering mechanisms [34, 48, 61]. Moreover, the increase of θ_{SH} with ρ_{xx} (Figure 5e) supports a dominant role of side-jump scattering and/or disorder-enhanced intrinsic contributions [37]. In metals with strong spin-orbit coupling, the anomalous Hall effect (AHE) scales with ρ_{xx} either linearly (extrinsic skew scattering) or quadratically (extrinsic side-jump scattering or

intrinsic mechanisms) [62]. Recent studies have established that SHE shares this scaling behavior [63]. The observed quadratic dependence of θ_{SH} on ρ_{xx} hints at the contribution of bulk-extrinsic side-jump scattering (Figure 5e) and rules out significant interfacial Bi effects on SHE, as confirmed by TEM and consistent with bulk alloy characteristics. To further confirm the mechanism, the intrinsic SHE contribution was subtracted, revealing $\rho_{\text{imp}}^{\text{SH}} \propto \rho_{\text{imp}}^2$ (Figure 5f), indicative of extrinsic side-jump scattering dominance [32, 33, 39, 48, 56, 64]. Here, $\rho_{\text{imp}}^{\text{SH}}$ denotes the impurity-induced spin Hall resistivity, and ρ_{imp} the resistivity due to impurities (See Supporting Information S10 for details on mechanism of SHE, including the exclusion of skew scattering as a contributing mechanism, and the extraction method for $\rho_{\text{imp}}^{\text{SH}}$ and ρ_{imp}). Therefore, increasing Bi concentration in Pt enhances extrinsic side-jump scattering, substantially boosting θ_{SH} and reducing the threshold current I_{th} necessary to drive robust AO, thereby enabling energy-efficient SHNOs.

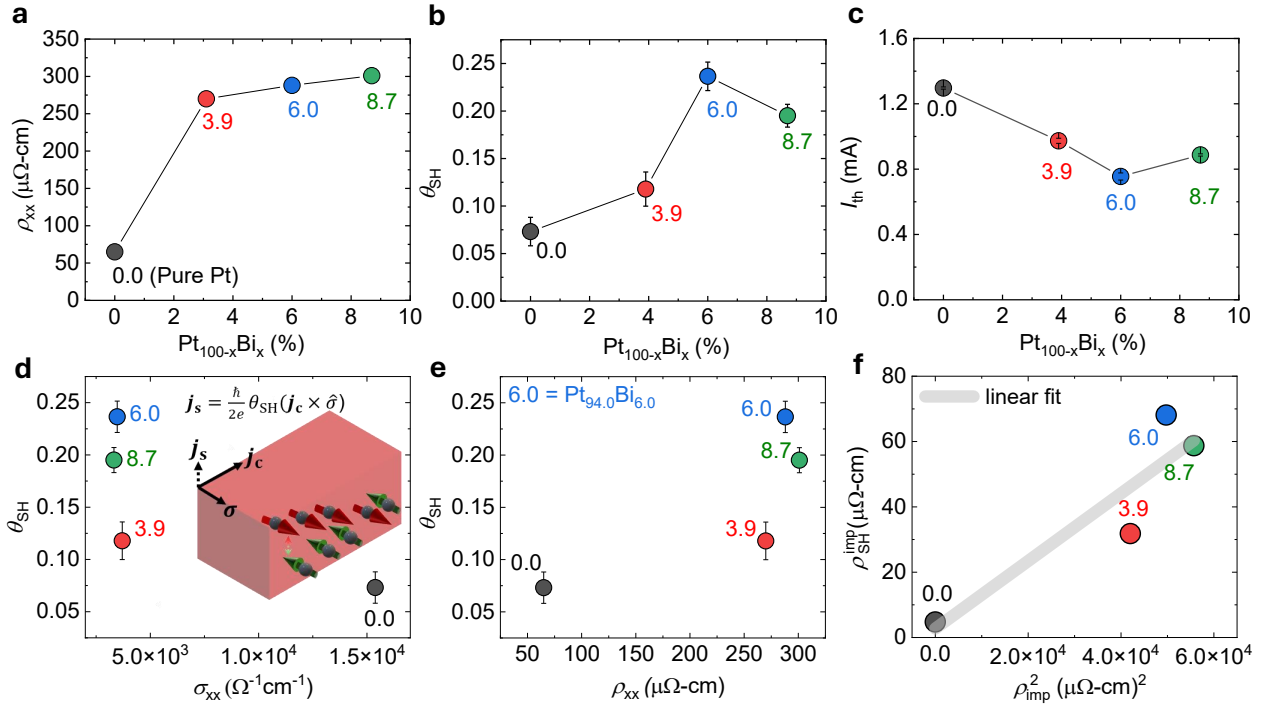


Figure 5: a) ρ_{xx} , b) θ_{SH} , and c) I_{th} versus Bi content x in $\text{Pt}_{100-x}\text{Bi}_x$ (wt.%). Error bars in (b) represent standard error from equation 2 and 4; in (c), mean deviation (MD) from I_{th} datasets (Supporting Information S7 for datasets; see Experimental Section for MD details). θ_{SH} plotted against d) σ_{xx} and e) ρ_{xx} . Inset in (d) shows bulk SHE schematic in PtBi alloy. f) $\rho_{\text{imp}}^{\text{SH}}$ as a function of ρ_{imp}^2 with linear fits as a solid line.

3 Conclusion

In summary, we demonstrate that Bi doping in Pt enhances θ_{SH} by over threefold and substantially reduces the threshold current I_{th} in SHNOs, enabling a superior ρ_{xx} trade-off crucial for low-power spintronic applications. The concurrent enhancement of θ_{SH} and

reduction in I_{th} underscores the reciprocal relationship between the spin Hall effect and auto-oscillations, as revealed by complementary ST-FMR and AO measurements. Furthermore, angular-dependent ST-FMR confirms a $\sin 2\phi \cos \phi$ symmetry across all $\text{Pt}_{100-x}\text{Bi}_x$ alloys, indicative of a bulk-origin, conventional spin-orbit torque mechanism. GIXRD analysis confirms that increased Bi doping in Pt leads to progressive reduction in crystallinity, significant peak broadening, and preferred crystallographic orientation, indicating structural modifications in the $\text{Pt}_{100-x}\text{Bi}_x$ alloys. These findings are corroborated by cross-sectional TEM, which reveals a uniform distribution of Bi throughout the Pt layer and a concurrent loss of crystallinity of Pt. The non-linear dependence of θ_{SH} on σ_{xx} and ρ_{xx} further reveals a $\rho_{\text{imp}}^{\text{SH}} \propto \rho_{\text{imp}}^2$ scaling, confirming extrinsic side-jump scattering as the dominant mechanism behind the enhanced SHE. Collectively, our findings establish a framework for energy-efficient spintronics beyond conventional 5d transition metals. By demonstrating Bi alloying with Pt as an effective strategy for enhancing charge-to-spin conversion, our work offers design principles for next-generation neuromorphic computing, SOT-MRAM, Ising machines, and GHz spintronic devices.

4 Experimental Section

4.1 Thin film preparation

High-resistance silicon (HR-Si) wafers ($> 10,000 \Omega \cdot \text{cm}$) were used as substrates. The $\text{Pt}_{100-x}\text{Bi}_x(4.0 \text{ nm})/\text{Co}_{40}\text{Fe}_{40}\text{B}_{20}(3.0 \text{ nm})$ were grown on HR-Si/Ta(2.4 nm), and further protected with a capping layer of $\text{MgO}(2.0 \text{ nm})/\text{SiO}_2(3.0 \text{ nm})$. Ta and $\text{Co}_{40}\text{Fe}_{40}\text{B}_{20}$ were sputtered at 11 W with 0.25 sccm Ar flow at a base pressure of 4×10^{-8} mbar, rising to 4×10^{-3} mbar during deposition. Other layers were deposited via electron beam evaporation. $\text{Pt}_{100-x}\text{Bi}_x$ was synthesized in situ by co-evaporation, with deposition rates monitored using a quartz crystal microbalance (QCM). The Bi source was stabilized before Pt adjustment. The deposition rate ratio required to achieve the desired $\text{Pt}_{100-x}\text{Bi}_x$ composition was calculated as: $\frac{v_a}{v_b} = \frac{M_a \rho_b}{M_b \rho_a} \cdot r$, where v_a and v_b are the deposition rates, M_a and M_b are the molar masses, ρ_a and ρ_b are the material densities, and r is the target molar ratio [44].

4.2 Grazing Incidence X-ray Diffraction (GIXRD)

GIXRD measurements were used to determine the full-width-at-half-maximum (FWHM) of the diffraction peaks. Data were acquired using a Mat:Nordic SAXSLAB instrument with a Rigaku 003 microfocusing Cu X-ray source (parallel beam from a two-bounce monochromator) and two Dectris detectors: Pilatus3 300K R (orthogonal) and 100K (goniometer circle). The beam path was evacuated to suppress air scattering, and a 1° incidence angle was employed to maximized signal intensity. Two-dimensional diffraction images were processed using SAXSGUI. FWHM values and lattice parameters were determined using TOPAS v6 (Bruker AXS, 2016), applying a pure platinum ($\text{Fm}\bar{3}\text{m}$) structural model and a pseudo-Voigt (PVII) profile. Peak broadening was analyzed separately. Exposure time was 3h per sample. Instrumental broadening was assessed using LaB6 powder.

4.3 Cross-sectional high-resolution TEM and HAADF-STEM imaging

TEM measurements were carried out using a JEOL monochromatic ARM200F microscope, which is equipped with a Schottky field emission gun, a double-Wien monochromator, a probe aberration corrector, an image aberration corrector, a Gatan image filter (GIF) Continuum, a Gatan Oneview camera, as well as a double silicon drift detector (SDD) for energy dispersive X-ray spectroscopy (EDS). The microscope was operated at 200 kV for the TEM measurements. TEM specimens were prepared by using a FEI Versa 3D focus ion beam-scanning electron microscope (FIB-SEM). After depositing a protection layer containing Pt and C using first the electron beam and then the Ga ion beam in the FIB-SEM, a lamella of the material was cut out using an ion beam at 30 kV and 1 nA. After transferring the lamella to a Cu TEM grid, the lamella was gradually thinned down by the ion beam. The thinning process was performed first at 30 kV and with a gradually decreasing beam current from 1 nA to 100 pA. Then, the gentle polishing of the specimen was carried out with an ion beam energy of 5 kV and 2 kV to minimize ion beam effect.

4.4 Device Fabrication

ST-FMR bars ($14 \times 4 \mu m^2$) and SHNOs with width of 100 nm were fabricated via electron-beam lithography (Raith EBPG 5200), followed by Ar-ion milling. The GSG-CPW contact pads were subsequently fabricated by mask-less ultraviolet lithography (Heidelberg Instruments MLA 150) and a lift-off technique, followed by Cu(800 nm)/Pt(20 nm) electrodes, deposited by DC magnetron sputtering. Detailed fabrication process can be found in Ref. [65].

4.5 ST-FMR and Auto-oscillation (AO) measurements

For ST-FMR, signal generator (RSSMB 100 A) was used to generate I_{rf} and the ST-FMR voltage V_{dc} was detected using a lock-in amplifier (SR830). For AO, I_{dc} was applied using Keithley 2400 sourcemeter and AO signal was then amplified by a low noise Amplifier (LNF LNR4 14B), and observed using a spectrum analyser (RSFSV) with a resolution bandwidth of 1 MHz. All measurements were performed at room temperature.

4.6 Statistical Analysis

The mean deviation (MD) quantifies dispersion in a dataset x_1, x_2, \dots, x_n and is computed with respect to the mean (\bar{x}) or median (M). The mean deviation about the mean is: $MD_{\bar{x}} = \frac{1}{n} \sum_{i=1}^n |x_i - \bar{x}|$, where \bar{x} is the arithmetic mean, $\bar{x} = \frac{1}{n} \sum_{i=1}^n x_i$. Here, $|x_i - \bar{x}|$ represents the absolute deviation from the mean.

Supporting Information Supporting Information is available from the corresponding authors upon request.

Acknowledgements Financial support from the Horizon 2020 research and innovation programme (Grant Nos. 899559 “SpinAge” and 835068 “TOPSPIN”), and the Swedish Research Council (VR Grant No. 2024-01943), is gratefully acknowledged. Financial support from the Swedish Research Council (VR) and the Swedish Foundation for Strategic Research (SSF) for access to ARTEMI, the Swedish National Infrastructure in Advanced Electron Microscopy (Grant Nos. 2021-00171 and RIF21-0026), is also acknowledged. This work was performed in part at the Chalmers Material Analysis Laboratory (CMAL). We thank Dr. Michał Strach (CMAL) for his assistance and insightful discussions regarding the GIXRD measurements.

Conflict of Interest

The authors declare no competing interests.

Authors’ contributions

US, AK, TSP, MM and JÅ initiated the idea and planned the study. HH prepared the thin films with input from TSP and AK. AK fabricated the devices. US performed all electrical auto-oscillations, spin-orbit torque measurements, and analysis with input from AK and MR. LJZ and ABY performed TEM measurements with input from EO. JÅ and MM coordinated and supervised the project. All authors contributed to the data analysis and interpretation of the results and co-wrote the manuscript.

Data Availability Statement

The data that support the findings of this study are available from the corresponding authors upon reasonable request.

References

- [1] Qiming Shao, Peng Li, Luqiao Liu, Hyunsoo Yang, Shunsuke Fukami, Armin Razavi, Hao Wu, Kang Wang, Frank Freimuth, Yuriy Mokrousov, et al. Roadmap of spin-orbit torques. *IEEE Transactions on Magnetics*, 57(7):1–39, 2021.
- [2] JE Hirsch. Spin hall effect. *Physical review letters*, 83(9):1834, 1999.
- [3] Mikhail I Dyakonov and VI Perel. Current-induced spin orientation of electrons in semiconductors. *Physics Letters A*, 35(6):459–460, 1971.
- [4] B. Dieny, I. L. Prejbeanu, K. Garello, P. Gambardella, P. Freitas, et al. Opportunities and challenges for spintronics in the microelectronics industry. *Nat. Electron.*, 3(8):446–459, Aug 2020.
- [5] Luqiao Liu, Chi-Feng Pai, Y. Li, H. W. Tseng, D. C. Ralph, and R. A. Buhrman. Spin-Torque Switching with the Giant Spin Hall Effect of Tantalum. *Science*, 336:555–558, 2012.

- [6] Guoqiang Yu, Pramey Upadhyaya, Yabin Fan, Juan G Alzate, Wanjun Jiang, Kin L Wong, So Takei, Scott A Bender, Li-Te Chang, Ying Jiang, et al. Switching of perpendicular magnetization by spin-orbit torques in the absence of external magnetic fields. *Nat. Nanotechnol.*, 9(7):548–554, 2014.
- [7] Ioan Mihai Miron, Kevin Garello, Gilles Gaudin, Pierre-Jean Zermatten, Marius V Costache, Stéphane Auffret, Sébastien Bandiera, Bernard Rodmacq, Alain Schuhl, and Pietro Gambardella. Perpendicular switching of a single ferromagnetic layer induced by in-plane current injection. *Nature*, 476(7359):189–193, 2011.
- [8] K Cai, G Talmelli, K Fan, S Van Beek, V Kateel, M Gupta, MG Monteiro, M Ben Chroud, G Jayakumar, A Trovato, et al. First demonstration of field-free perpendicular sot-mram for ultrafast and high-density embedded memories. In *2022 International Electron Devices Meeting (IEDM)*, pages 36–2. IEEE, 2022.
- [9] Himanshu Fulara, Mohammad Zahedinejad, Roman Khymyn, AA Awad, Shreyas Muralidhar, Mykola Dvornik, and Johan Åkerman. Spin-orbit torque-driven propagating spin waves. *Science advances*, 5(9):eaax8467, 2019.
- [10] Akash Kumar, Avinash Kumar Chaurasiya, Victor H González, Nilamani Behera, Ademir Alemán, Roman Khymyn, Ahmad A Awad, and Johan Åkerman. Spin-wave-mediated mutual synchronization and phase tuning in spin hall nano-oscillators. *Nature Physics*, 21:245–252, 2025.
- [11] VE Demidov, S Urazhdin, A Zholud, AV Sadovnikov, and SO Demokritov. Nanoconstriction-based spin-hall nano-oscillator. *Applied Physics Letters*, 105(17), 2014.
- [12] Akash Kumar, Artem Litvinenko, Nilamani Behera, Ahmad A Awad, Roman Khymyn, and Johan Åkerman. Mutual synchronization in spin-torque and spin hall nano-oscillators. *Nanomagnets as Dynamical Systems: Physics and Applications*, pages 143–182, 2024.
- [13] Satoru Emori, Uwe Bauer, Sung-Min Ahn, Eduardo Martinez, and Geoffrey SD Beach. Current-driven dynamics of chiral ferromagnetic domain walls. *Nature materials*, 12(7):611–616, 2013.
- [14] Nirel Bernstein, Hang Li, Benjamin Assouline, Yong-Chang Lau, Igor Rozhansky, Wenhong Wang, and Amir Capua. Spin-torque skyrmion resonance in a frustrated magnet. *Nat. Commun.*, 16(1):1–9, 2025.
- [15] AV Khvalkovskiy, V Cros, D Apalkov, V Nikitin, M Krounbi, KA Zvezdin, A Anane, J Grollier, and A Fert. Matching domain-wall configuration and spin-orbit torques for efficient domain-wall motion. *Phys. Rev. B*, 87(2):020402, 2013.
- [16] Luqiao Liu, Takahiro Moriyama, D_C Ralph, and R_A Buhrman. Spin-torque ferromagnetic resonance induced by the spin hall effect. *Physical review letters*, 106(3):036601, 2011.

- [17] RH Liu, WL Lim, and S Urazhdin. Spectral characteristics of the microwave emission by the spin hall nano-oscillator. *Physical review letters*, 110(14):147601, 2013.
- [18] Shinya Kasai, Kouta Kondou, Hiroaki Sukegawa, Seiji Mitani, Kazuhito Tsukagoshi, and Yoshichika Otani. Modulation of effective damping constant using spin hall effect. *Applied Physics Letters*, 104(9), 2014.
- [19] Tingsu Chen, Randy K Dumas, Anders Eklund, Pranaba K Muduli, Afshin Houshang, Ahmad A Awad, Philipp Dürrenfeld, B Gunnar Malm, Ana Rusu, and Johan Åkerman. Spin-torque and spin-hall nano-oscillators. *Proceedings of the IEEE*, 104(10):1919–1945, 2016.
- [20] AA Awad, Ph Dürrenfeld, A Houshang, M Dvornik, Ezio Iacocca, RK Dumas, and Johan Åkerman. Long-range mutual synchronization of spin hall nano-oscillators. *Nature Physics*, 13(3):292–299, 2017.
- [21] Akash Kumar, Himanshu Fulara, Roman Khymyn, Artem Litvinenko, Mohammad Zahedinejad, Mona Rajabali, Xiaotian Zhao, Nilamani Behera, Afshin Houshang, Ahmad A Awad, et al. Robust mutual synchronization in long spin hall nano-oscillator chains. *Nano Letters*, 23(14):6720–6726, 2023.
- [22] Mohammad Zahedinejad, Ahmad A Awad, Shreyas Muralidhar, Roman Khymyn, Himanshu Fulara, Hamid Mazraati, Mykola Dvornik, and Johan Åkerman. Two-dimensional mutually synchronized spin hall nano-oscillator arrays for neuromorphic computing. *Nature nanotechnology*, 15(1):47–52, 2020.
- [23] Nilamani Behera, Avinash Kumar Chaurasiya, Victor H González, Artem Litvinenko, Lakhan Bainsla, Akash Kumar, Roman Khymyn, Ahmad A Awad, Himanshu Fulara, and Johan Åkerman. Ultra-low current 10 nm spin hall nano-oscillators. *Advanced Materials*, 36(5):2305002, 2024.
- [24] Nilamani Behera, Avinash Kumar Chaurasiya, Akash Kumar, Roman Khymyn, Artem Litvinenko, Lakhan Bainsla, Ahmad A Awad, and Johan Åkerman. Ultra-large mutually synchronized networks of 10 nm spin hall nano-oscillators. *arXiv preprint arXiv:2501.18321*, 2025.
- [25] Mohammad Zahedinejad, Himanshu Fulara, Roman Khymyn, Afshin Houshang, Mykola Dvornik, Shunsuke Fukami, Shun Kanai, Hideo Ohno, and Johan Åkerman. Memristive control of mutual spin hall nano-oscillator synchronization for neuromorphic computing. *Nature materials*, 21(1):81–87, 2022.
- [26] Jacob Torrejon, Mathieu Riou, Flavio Abreu Araujo, Sumito Tsunegi, Guru Khalsa, Damien Querlioz, Paolo Bortolotti, Vincent Cros, Kay Yakushiji, Akio Fukushima, et al. Neuromorphic computing with nanoscale spintronic oscillators. *Nature*, 547(7664):428–431, 2017.
- [27] Julie Grollier, Damien Querlioz, KY Camsari, Karin Everschor-Sitte, Shunsuke Fukami, and Mark D Stiles. Neuromorphic spintronics. *Nature electronics*, 3(7):360–370, 2020.

- [28] Afshin Houshang, Mohammad Zahedinejad, Shreyas Muralidhar, Jakub Chęciński, Roman Khymyn, Mona Rajabali, Himanshu Fulara, Ahmad A Awad, Mykola Dvornik, and Johan Åkerman. Phase-binarized spin hall nano-oscillator arrays: Towards spin hall ising machines. *Physical Review Applied*, 17(1):014003, 2022.
- [29] Jong-Guk Choi, Jaehyeon Park, Min-Gu Kang, Doyoon Kim, Jae-Sung Rieh, Kyung-Jin Lee, Kab-Jin Kim, and Byong-Guk Park. Voltage-driven gigahertz frequency tuning of spin hall nano-oscillators. *Nature communications*, 13(1):3783, 2022.
- [30] Yi Wang, Praveen Deorani, Xuepeng Qiu, Jae Hyun Kwon, and Hyunsoo Yang. Determination of intrinsic spin hall angle in pt. *Applied Physics Letters*, 105(15), 2014.
- [31] Utkarsh Shashank, Rohit Medwal, Taiga Shibata, Razia Nongjai, Joseph Vimal Vas, Martial Duchamp, Kandasami Asokan, Rajdeep Singh Rawat, Hironori Asada, Surbhi Gupta, et al. Enhanced spin hall effect in s-implanted pt. *Advanced Quantum Technologies*, 4(1):2000112, 2021.
- [32] Utkarsh Shashank, Rohit Medwal, Yoji Nakamura, John Rex Mohan, Razia Nongjai, Asokan Kandasami, Rajdeep Singh Rawat, Hironori Asada, Surbhi Gupta, and Yasuhiro Fukuma. Highly dose dependent damping-like spin-orbit torque efficiency in o-implanted pt. *Applied Physics Letters*, 118(25), 2021.
- [33] Utkarsh Shashank, Yoji Nakamura, Yu Kusaba, Takafumi Tomoda, Razia Nongjai, Asokan Kandasami, Rohit Medwal, Rajdeep Singh Rawat, Hironori Asada, Surbhi Gupta, et al. Disentanglement of intrinsic and extrinsic side-jump scattering induced spin hall effect in n-implanted pt. *Phys. Rev. B*, 107(6):064402, 2023.
- [34] Utkarsh Shashank, Takafumi Tomoda, Arun Jacob Mathew, Garima Vashisht, Koki Imai, Yu Kusaba, Chung-Li Dong, Chi-Liang Chen, Yoichi Horibe, Manabu Ishimaru, et al. Giant spin-orbit torque induced by spin hall effect in amorphous pt (p) alloys. *NPG Asia Materials*, 17(1):15, 2025.
- [35] Liupeng Yang, Yining Fei, Kaiyuan Zhou, Lina Chen, Qingwei Fu, Liyuan Li, Chunjie Yan, Haotian Li, Youwei Du, and Ronghua Liu. Maximizing spin-orbit torque efficiency of ta (o)/py via modulating oxygen-induced interface orbital hybridization. *Applied Physics Letters*, 118(3), 2021.
- [36] Kai-Uwe Demasius, Timothy Phung, Weifeng Zhang, Brian P Hughes, See-Hun Yang, Andrew Kellock, Wei Han, Aakash Pushp, and Stuart SP Parkin. Enhanced spin-orbit torques by oxygen incorporation in tungsten films. *Nature communications*, 7(1):10644, 2016.
- [37] Tian-Yue Chen, Chun-Te Wu, Hung-Wei Yen, and Chi-Feng Pai. Tunable spin-orbit torque in cu-ta binary alloy heterostructures. *Physical Review B*, 96(10):104434, 2017.
- [38] Peng Wang, Andrea Migliorini, See-Hun Yang, Jae-Chun Jeon, Ilya Kostanovskiy, Holger Meyerheim, Hyeon Han, Hakan Deniz, and Stuart SP Parkin. Giant spin hall effect and spin-orbit torques in 5d transition metal-aluminum alloys from extrinsic scattering. *Advanced Materials*, 34(23):2109406, 2022.

- [39] Rajagopalan Ramaswamy, Yi Wang, Mehrdad Elyasi, M Motapothula, T Venkatesan, Xuepeng Qiu, and Hyunsoo Yang. Extrinsic spin hall effect in cu 1- x pt x. *Physical Review Applied*, 8(2):024034, 2017.
- [40] X Zhou, M Tang, XL Fan, XP Qiu, and SM Zhou. Disentanglement of bulk and interfacial spin hall effect in ferromagnet/normal metal interface. *Phys. Rev. B*, 94(14):144427, 2016.
- [41] Caiyun Hong, Lichuan Jin, Huaiwu Zhang, Mingming Li, Yiheng Rao, Bo Ma, Jialu Li, Zhiyong Zhong, and Qinghui Yang. Giant inverse spin hall effect in bi doped ptbi alloy. *Advanced Electronic Materials*, 4(8):1700632, 2018.
- [42] Nilamani Behera, Himanshu Fulara, Lakhan Bainsla, Akash Kumar, Mohammad Zahedinejad, Afshin Houshang, and Johan Åkerman. Energy-efficient $W_{100-x}Ta_x/Co-Fe-B/MgO$ spin Hall nano-oscillators. *Phys. Rev. Appl.*, 18(2):024017, 2022.
- [43] Zhendong Chi, Yong-Chang Lau, Masashi Kawaguchi, and Masamitsu Hayashi. Charge-spin conversion in pt1- xbix alloys for spin-orbit torque switching. *APL Materials*, 9(6), 2021.
- [44] Tristan Joachim Winkel, Tahereh Sadat Parvini, Finn-Frederik Stiewe, Jakob Walowski, Farshad Moradi, and Markus Münzenberg. Comparative analysis of thz signal emission from bilayer heterostructures: Wideband and high-frequency thz signal advantage of ptbi-based emitter. *Applied Physics Letters*, 124(1), 2024.
- [45] Ya Feng, Qi Jiang, Baojie Feng, Meng Yang, Tao Xu, Wenjing Liu, Xiufu Yang, Masashi Arita, Eike F Schwier, Kenya Shimada, et al. Rashba-like spin splitting along three momentum directions in trigonal layered ptbi2. *Nat. Commun.*, 10(1):4765, 2019.
- [46] Sebastian Schimmel, Yanina Fasano, Sven Hoffmann, Julia Besproswanny, Laura Teresa Corredor Bohorquez, Joaquín Puig, Bat-Chen Elshalem, Beena Kalisky, Grigory Shipunov, Danny Baumann, et al. Surface superconductivity in the topological weyl semimetal t-ptbi2. *Nat. Commun.*, 15(1):9895, 2024.
- [47] Yong-Chang Lau, Takeshi Seki, and Koki Takanashi. Highly fcc-textured pt-al alloy films grown on mgo (001) showing enhanced spin hall efficiency. *APL Materials*, 9(8), 2021.
- [48] Utkarsh Shashank, Yu Kusaba, Junnosuke Nakamura, Arun Jacob Mathew, Koki Imai, Shinya Senba, Hironori Asada, and Yasuhiro Fukuma. Charge-spin interconversion in nitrogen sputtered pt via extrinsic spin hall effect. *Journal of Physics: Condensed Matter*, 36(32):325802, 2024.
- [49] A Hecq, JP Delrue, M Hecq, and T Robert. Sputtering deposition, xps and x-ray diffraction characterization of hard nitrogen-platinum thin films. *Journal of Materials Science*, 16:407–412, 1981.

- [50] WL Peng, JY Zhang, GN Feng, XL Xu, C Yang, YL Jia, and GH Yu. Tunable damping-like and field-like spin-orbit-torque in pt/co/hfo2 films via interfacial charge transfer. *Applied Physics Letters*, 115(17), 2019.
- [51] Xin Fan, Halise Celik, Jun Wu, Chaoying Ni, Kyung-Jin Lee, Virginia O Lorenz, and John Q Xiao. Quantifying interface and bulk contributions to spin-orbit torque in magnetic bilayers. *Nature communications*, 5(1):3042, 2014.
- [52] Tianxiang Nan, Satoru Emori, Carl T Boone, Xinjun Wang, Trevor M Oxholm, John G Jones, Brandon M Howe, Gail J Brown, and Nian X Sun. Comparison of spin-orbit torques and spin pumping across nife/pt and nife/cu/pt interfaces. *Physical Review B*, 91(21):214416, 2015.
- [53] Michael Harder, Yongsheng Gui, and Can-Ming Hu. Electrical detection of magnetization dynamics via spin rectification effects. *Physics Reports*, 661:1–59, 2016.
- [54] John Rex Mohan, Utkarsh Shashank, Angshuman Deka, Takayasu Hanashima, Rohit Medwal, Surbhi Gupta, Rajdeep Singh Rawat, Hironori Asada, and Yasuhiro Fukuma. Observation of out-of-plane antidamping torque at the platinum/permalloy interface. *ACS Applied Materials & Interfaces*, 2025.
- [55] Lakhan Bainsla, Akash Kumar, Ahmad A Awad, Chunlei Wang, Mohammad Zahedinejad, Nilamani Behera, Himanshu Fulara, Roman Khymyn, Afshin Houshang, Jonas Weissenrieder, et al. Ultrathin ferrimagnetic gdfeco films with low damping. *Advanced Functional Materials*, 32(23):2111693, 2022.
- [56] Akash Kumar, Rajni Bansal, Sujeet Chaudhary, and Pranaba Kishor Muduli. Large spin current generation by the spin hall effect in mixed crystalline phase ta thin films. *Phys. Rev. B*, 98(10):104403, 2018.
- [57] Yi Wang, Rajagopalan Ramaswamy, and Hyunsoo Yang. Fmr-related phenomena in spintronic devices. *Journal of Physics D: Applied Physics*, 51(27):273002, 2018.
- [58] Kouta Kondou, Hua Chen, Takahiro Tomita, Muhammad Ikhlas, Tomoya Higo, Allan H MacDonald, Satoru Nakatsuji, and YoshiChika Otani. Giant field-like torque by the out-of-plane magnetic spin hall effect in a topological antiferromagnet. *Nature communications*, 12(1):6491, 2021.
- [59] C. Kittel. On the theory of ferromagnetic resonance absorption. *Phys. Rev.*, 73:155, Jan 1948.
- [60] Mykola Dvornik, Ahmad A Awad, and Johan Åkerman. Origin of magnetization auto-oscillations in constriction-based spin hall nano-oscillators. *Physical Review Applied*, 9(1):014017, 2018.
- [61] Edurne Sagasta, Yasutomo Omori, Miren Isasa, Martin Gradhand, Luis E Hueso, Yasuhiro Niimi, YoshiChika Otani, and Fèlix Casanova. Tuning the spin hall effect of pt from the moderately dirty to the superclean regime. *Physical Review B*, 94(6):060412, 2016.

- [62] Qiang Hao and Gang Xiao. Giant spin hall effect and magnetotransport in a ta/cofeb/mgo layered structure: A temperature dependence study. *Physical Review B*, 91(22):224413, 2015.
- [63] Jairo Sinova, Sergio O. Valenzuela, J. Wunderlich, C.H. Back, and T. Jungwirth. Spin Hall effects. *Rev. Mod. Phys.*, 87(4):1213–1260, October 2015.
- [64] R Asomoza, A Fert, and R Reich. Gadolinium-heavy rare earth alloys: preparation, metallographic study and extraordinary hall effect. *Journal of the Less Common Metals*, 90(2):177–201, 1983.
- [65] Akash Kumar, Mona Rajabali, Victor Hugo González, Mohammad Zahedinejad, Afshin Houshang, and Johan Åkerman. Fabrication of voltage-gated spin Hall nano-oscillators. *Nanoscale*, 14:1432–1439, 2022.